Ligand protons in a frozen solution of copper histidine relax via a T_{1e}-driven three-spin mechanism

S. Stoll[a)]
Physical Chemistry Laboratory, ETH Zurich, 8093 Zurich, Switzerland

B. Epel,[b)] S. Vega, and D. Goldfarb
Department of Chemical Physics, Weizmann Institute of Science, Rehovot 76100, Israel

(Received 16 May 2007; accepted 11 September 2007; published online 30 October 2007)

Davies electron-nuclear double resonance spectra can exhibit strong asymmetries for long mixing times, short repetition times, and large thermal polarizations. These asymmetries can be used to determine nuclear relaxation rates in paramagnetic systems. Measurements of frozen solutions of copper(*L*-histidine)$_2$ reveal a strong field dependence of the relaxation rates of the protons in the histidine ligand, increasing from low ($g_{\|}$) to high ($g_{\perp}$) field. It is shown that this can be attributed to a concentration-dependent T_{1e}-driven relaxation process involving strongly mixed states of three spins: the histidine proton, the Cu(II) electron spin of the same complex, and another distant electron spin with a resonance frequency differing from the spectrometer frequency approximately by the proton Larmor frequency. The protons relax more efficiently in the $g_{\perp}$ region, since the number of distant electrons able to participate in this relaxation mechanism is higher than in the $g_{\|}$ region. Analytical expressions for the associated nuclear polarization decay rate T_{een}^{-1} are developed and Monte Carlo simulations are carried out, reproducing both the field and the concentration dependences of the nuclear relaxation. © *2007 American Institute of Physics*.
[DOI: 10.1063/1.2794329]

I. INTRODUCTION

Pulse electron-nuclear double resonance (ENDOR) measurements at high frequencies/fields[1–4] offer a number of advantages over conventional *X*-band frequencies, among which are (i) better frequency separation of nuclei with different gyromagnetic ratios γ; (ii) a wider applicability of the first-order expressions for the ENDOR frequencies which facilitates data analysis; (iii) a higher nuclear Larmor frequency, which facilitates measurements of weakly coupled low-γ nuclei such as deuterium; (iv) a high thermal polarization, which makes it possible to determine the signs of hyperfine coupling constants[5] and provides a means to measure nuclear relaxation.[6]

In this work we use two-dimensional variations of the standard Davies ENDOR experiment, carried out at 94.9 GHz, to measure the nuclear relaxation rates of the α-protons in the histidine ligands of Cu(*L*-histidine)$_2$ in a frozen D_2O/glycerol solution (CuHis). In particular, we explore the dependence of the nuclear relaxation rate on the applied magnetic field, within the field range spanning the electron paramagnetic resonance (EPR) powder pattern, and on the concentration. The present study was motivated by the observation that for a number of Cu(II) complexes the low-temperature 94.9 GHz ENDOR spectra were more often asymmetric (i.e., the α and the β peaks have different intensities) when the measurements were carried out at the $g_{\|}$ field position than at the $g_{\perp}$ field position.[7,8]

In our study, the ^{1}H relaxation rates obtained from the ENDOR experiments are not much slower than the electron spin-lattice relaxation rate and exhibit a strong field and concentration dependence. We have examined several relaxation mechanisms that can possibly account for these dependencies and have identified one that explains all trends and predicts the correct orders of magnitude of the nuclear relaxation constants. Thus, these high-field ENDOR experiments provide some new insight into the mechanisms that govern nuclear relaxation in paramagnetic systems at high fields.

This work also relates to nuclear polarization transfer mechanisms in dynamic nuclear polarization (DNP) at high fields.[9] There it has been observed that the DNP strength increases with the electron-electron cross relaxation rate and thus with concentration.[10–12] The mechanism outlined below can possibly offer additional insight into the working of the DNP cross effect.[13]

The paper is structured as follows. The next section describes the ENDOR sequences employed and summarizes the theoretical background for the determination of the relaxation constants from the spectra. In the two following sections, experimental methods and experimental results are presented. Section V discusses relaxation mechanisms that contribute to the observed relaxational behavior, and Sec. VI concludes.

[a)]Author to whom correspondence should be addressed. Present address: Department of Chemistry, University of California, Davis, CA 95616, USA. Electronic mail: sstoll@ucdavis.edu
[b)]Present address: Department of Radiation and Cellular Oncology, University of Chicago, Chicago, IL 60637, USA.

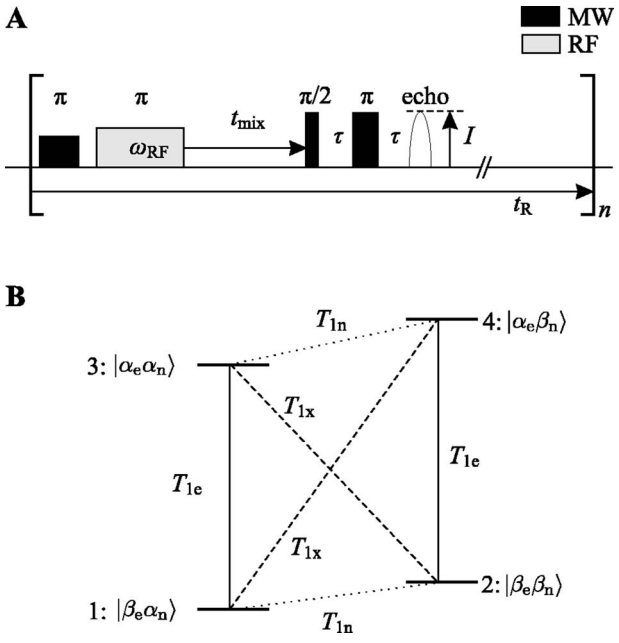

FIG. 1. Pulse sequences: (A) VMT (ω_{rf} and t_{mix} varied, t_R fixed) and VRT (ω_{rf} and t_R varied, t_{mix} fixed) Davies ENDOR experiments. (B) $S=I=1/2$ system with four levels connected by relaxation.

II. THEORETICAL BACKGROUND

In pulse ENDOR, the ENDOR spectrum is most commonly measured using the Davies or the Mims ENDOR sequences.[14] Figure 1(a) shows the Davies ENDOR sequences, where the echo amplitude I is measured as a function of ω_{rf}, the frequency of the radio frequency (rf) pulse. Two time intervals are of relevance for relaxational effects: t_{mix}, the time between the rf pulse and the two-pulse detection sequence, and t_R, the repetition time.

The Davies ENDOR spectrum of a spin-1/2 nucleus weakly coupled to an unpaired electron consists of two lines at the nuclear resonance frequencies ω_α and ω_β centered around the nuclear Larmor frequency ω_n. The line intensities are best given in terms of the ENDOR efficiencies F^α and F^β,

$$F^{\alpha,\beta}(t_{mix},t_R)=\frac{I^{off}(t_{mix},t_R)-I^{\alpha,\beta}(t_{mix},t_R)}{2I_0(t_R)}, \quad (1)$$

where I^{off} and $I^{\alpha,\beta}$ are the echo amplitudes obtained in the absence and presence of a rf pulse resonant with a nuclear transition in the α or β electron-spin manifold. I_0 is the echo amplitude in a two-pulse echo experiment with the same τ and t_R values as used in the ENDOR experiment.

In the standard ENDOR experiment, t_{mix} is set to a minimum in order not to lose the ENDOR signal due to relaxation, and t_R is chosen to be sufficiently long as to allow all spins to completely regain thermal equilibrium between pulse sequences. In this standard case, the high-field ^{1}H ENDOR spectrum is symmetric, i.e., the peaks at the nuclear frequencies ω_α and ω_β are of equal intensity.

If t_{mix} is prolonged, relaxation can take place in the time between the rf pulse and the two-pulse detection sequence, and, as a consequence, the ENDOR spectrum gets weaker and can become asymmetric. ENDOR peaks belonging to the α electron-spin manifold ($m_S=+1/2$) partially or fully invert with increasing t_{mix}, while those belonging to the β manifold remain positive.[6] If t_R is shortened, the time between sequences can become too short for the spins to reach thermal equilibrium. Again, the ENDOR spectrum becomes weaker and asymmetric, as nuclear polarization generated in one sequence survives until the next one. Now it is the ENDOR peaks belonging to the β electron-spin manifold ($m_S=-1/2$) that lose intensity and eventually invert with decreasing t_R.[6]

Recording the Davies ENDOR spectrum as a function of t_{mix} or t_R (Ref. 6) results in two two-dimensional experiments: The variable mixing time (VMT) experiment (ω_{rf} and t_{mix} swept, t_R long) and the variable repetition time (VRT) experiment (ω_{rf} and t_R swept, t_{mix} short). From both experiments, nuclear relaxation rates can be obtained.

A very simple kinetic model[6] describing the time evolution of the populations in a four-level system ($S=1/2$, $I=1/2$) was used to calculate the dependence of $F^{\alpha,\beta}$ on the thermal polarization and on the electron and nuclear spin-lattice and cross relaxation times, T_{1e}, T_{1n}, and T_{1x}, respectively [see Fig. 1(b)].

In this model, all coherences are neglected and the populations n_i of the four states i are represented by a column vector $\boldsymbol{n}=(n_1,n_2,n_3,n_4)^T$. The levels are numbered from the lowest to the highest in energy [see Fig. 1(b)]. All microwave (MW) and rf pulses are assumed to be selective, that is, each of them affects populations of only two levels. Pulse lengths and interpulse intervals except t_{mix} and t_R are neglected, as they are usually very short compared to T_{1e} and T_{1x}, which determine the time scale of the experiment. The time evolution of the population vector during t_{mix} and t_R is described by

$$\frac{d}{dt}\boldsymbol{n}(t)=-\Gamma_{en}\boldsymbol{n}(t), \quad (2)$$

with the asymmetric relaxation matrix,

$$\Gamma_{en}=\begin{pmatrix} \Gamma_n+\epsilon\Gamma_e+\epsilon\Gamma_x & -\Gamma_n & -\Gamma_e & -\Gamma_x \\ -\Gamma_n & \Gamma_n+\epsilon\Gamma_e+\epsilon\Gamma_x & -\Gamma_x & -\Gamma_e \\ -\epsilon\Gamma_e & -\epsilon\Gamma_x & \Gamma_n+\Gamma_e+\Gamma_x & -\Gamma_n \\ -\epsilon\Gamma_x & -\epsilon\Gamma_e & -\Gamma_n & \Gamma_n+\Gamma_e+\Gamma_x \end{pmatrix}. \quad (3)$$

Here it is assumed that the relaxation rates for the two forbidden EPR transitions (1-4 and 2-3) are identical. The relaxation times T_{1e}, T_{1n}, and T_{1x} are related to the elements in the relaxation matrix by[6]

$$T_{1e}^{-1} = (1+\epsilon)\Gamma_e, \quad T_{1n}^{-1} = 2\Gamma_n, \quad T_{1x}^{-1} = (1+\epsilon)\Gamma_x. \tag{4}$$

In paramagnetic systems, T_{1n} is, in general, much larger than T_{1x} and T_{1e}. For the rest of this work, we will thus assume $T_{1n}^{-1} \approx 0$ and $\Gamma_n \approx 0$. ϵ is the polarization factor at thermal equilibrium,

$$\epsilon = \exp\left(-\frac{\hbar\omega_{MW}}{k_B T}\right), \tag{5}$$

where $\omega_{MW} \approx \omega_{13}$ is the spectrometer frequency resonant with the transition 1-3 and T is the temperature. For the experimental conditions in the present work ($\omega_{MW}/2\pi = 94.9$ GHz and $T = 5.5$ K), $\epsilon = 0.44$. The population vector at thermal equilibrium is given by $\boldsymbol{n}_{eq} \propto (1,1,\epsilon,\epsilon)^T$. The echo amplitude I is taken as the population difference, $I = n_1 - n_3$, obtained from $\boldsymbol{n}$ immediately before the two-pulse echo detection sequence. $\boldsymbol{n}$ is calculated using $\boldsymbol{n}_{eq}$, the appropriate pulse propagators, and the relaxation matrix Γ_{en} given in Eq. (2), for the free evolution times t_{mix} and t_R.[6] The ENDOR efficiency is computed according to Eq. (1). A convenient measure of the ENDOR asymmetry is $\Delta F = |F^\alpha - F^\beta|$.

From numerical simulations using the above model, a few general properties regarding the VMT/VRT experiments and the ENDOR asymmetry can be derived. For the VMT experiment ($t_R \gg T_{1x}, T_{1e}$), $F^\alpha \leqslant F^\beta$ for all t_{mix} values. The α peak is inverted for $t_{mix} > \approx 3T_{1e}$ under the condition $T_{1x} > T_{1e}$. The VMT experiment is a double inversion recovery experiment: The polarizations on both an electron and a nuclear transition are inverted by the first two pulses. During t_{mix}, they relax and recover to their thermal equilibrium values. In the limit of long t_{mix}, where the spin system has relaxed to thermal equilibrium before the detection sequence, the ENDOR spectrum disappears and both F^α and F^β approach zero.

For the VRT experiment ($t_{mix} \ll T_{1x}, T_{1e}$), it is the β peak which can be weaker than the α peak, i.e., $F^\beta \leqslant F^\alpha$. The β peak appears inverted only for short repetition times $t_R < T_{1x}$ if $T_{1x} > 3T_{1e}$. The VRT experiment is an analog of a nuclear saturation recovery experiment. If t_R is shorter than the overall nuclear relaxation rate, both ENDOR peaks appear saturated, the β transition more than the α.

The VMT and VRT dependencies of the spectral asymmetry ΔF on the swept time intervals are similar in shape, with the VMT giving up to 20% larger asymmetries than the VRT. So, in general, an asymmetry is more easily observed in the VMT experiment.

Large thermal polarizations and long T_{1x} are the ingredients necessary for observing a significant ENDOR asymmetry. For a given set of relaxation times, the observable asymmetry is approximately proportional to ω_{MW}/T in its experimentally accessible range. For a given ω_{MW}/T, the asymmetry depends roughly linearly on $\log(T_{1x}/T_{1e})$ in the range of $1 < T_{1x}/T_{1e} < 10$. However, since T_{1x}/T_{1e} itself depends on the temperature and the spectrometer frequency, these two dependencies cannot be observed separately in an experiment.

To avoid relaxational asymmetry effects in ENDOR spectra and to maximize the signal, not only has t_{mix} to be as short as possible but also t_R must be long enough to permit complete relaxation of the *nuclear* polarizations, which is governed by T_{1x} and not by T_{1e}. In the case $T_{1x} \gg T_{1e}$, this imposes impractically long t_R. As a remedy, an additional rf π pulse can be placed *after* the echo.[15] This pulse restores the nuclear polarization to the state before the first rf pulse, and a t_R as short as a few T_{1e} can now be employed without weakening the measured ENDOR spectrum. Alternatively, stochastic acquisition can be used when collecting the ENDOR spectrum.[16,17] In this method, ω_{rf} is not incremented linearly from sequence to sequence, but set in random order so that two subsequent rf pulses in the acquisition have significantly different frequencies.

III. EXPERIMENTAL

Solutions of Cu(II)(*L*-histidine)$_2$ at *p*H 7.3 (CuHis) were prepared as reported in the literature.[7] The samples were prepared in D_2O/glycerol (1:1 v/v). In some samples, glycerol-d_3 was used. In this way, the protons of the amine group in histidine were exchanged for deuterium. All samples were degassed.

94.9 GHz pulse EPR and ENDOR measurements were carried out at 5.5 K using a homebuilt spectrometer.[18] Echo-detected (ED) EPR spectra were recorded using the two-pulse echo sequence ($\pi/2$-τ-π-τ-echo) where the echo intensity was recorded as a function of the magnetic field B_0. MW pulse lengths (t_{MW}) of 50 and 100 ns and an interpulse delay $\tau = 300$ ns were used. The magnetic field values were calibrated using the Larmor frequency of the solvent protons, ω_n, as obtained by Mims ENDOR measurements.

T_{1e} values across the EPR spectrum were determined by fitting a single exponential to recovery curves obtained by saturation recovery (t_{sat}-T-$\pi/2$-τ-π-τ-echo). The length of the saturation pulse was $t_{sat} = 10$ μs, while t_{MW} for the echo detection were 50 and 100 ns, respectively. In order to minimize the contributions of spectral diffusion to the recovery curve, the saturation pulse length was increased until no further change in the recovery curve was observed.

The ^{1}H ENDOR spectra were measured using the Davies ENDOR pulse sequence [see Fig. 1(a)]. The experimental conditions for the Davies ENDOR spectra were $t_{MW} = 200$, 100, 200 ns; $\tau = 500$ ns; $t_{rf} = 10$–15 μs.

VMT and VRT Davies ENDOR data based on the sequences shown in Fig. 1(a) were acquired for various magnetic field positions across the EPR spectrum, using the same settings as for the standard Davies ENDOR experiment. In the VMT experiments, the mixing time t_{mix} was varied between 0.5 and 10 ms in steps of 0.5 ms. The repetition time was set to 25 ms, a compromise between the long-t_R limit and a reasonably fast acquisition. In the VRT experiments, the mixing time was 40 μs and the repetition time t_R was swept from 10 up to 70 ms in steps of 1 ms. The lower

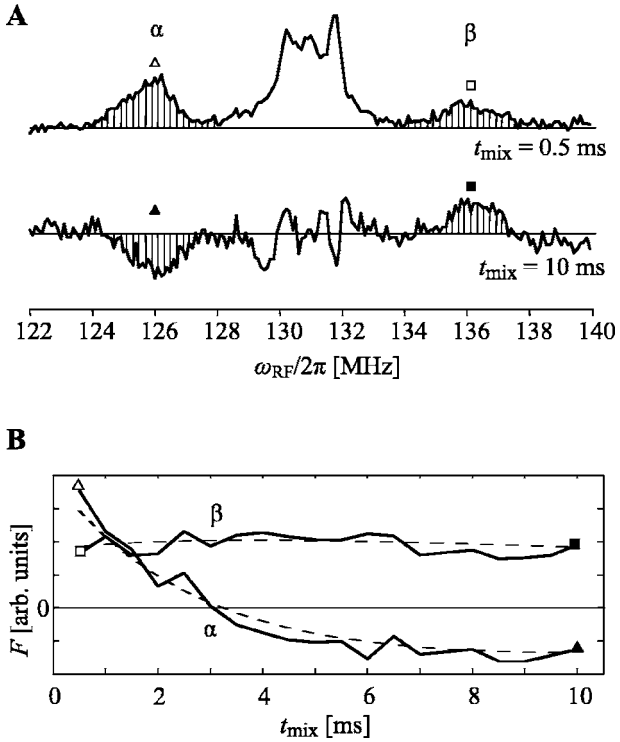

FIG. 2. (A) ^{1}H ENDOR spectra of CuHis recorded at 94.9 GHz and 3080 mT, t_{mix}=0.5 ms (top), 10 ms (bottom). The spectra were recorded at 5.5 K and with t_R=25 ms. The areas of the H_α peaks which were used to calculate $F^{\alpha,\beta}$ are shaded. (B) An illustration of the $F^{\alpha,\beta}(t_{mix})$ curves as obtained from the VMT experiment together with the least-squares fitted model used to determine T_{1x}.

bound for the repetition time was imposed by technical limitations. 30 repetitions were performed before the rf frequency was changed [n=30 in Fig. 1(a)].

The procedure of extracting T_{1x} from the VMT and VRT data is illustrated in Fig. 2. Intensities of the peaks of the H_α histidine protons were obtained by integrating the area under the peaks [shaded areas in Fig. 2(a)]. The dependence of these areas on t_{mix} or t_R [Fig. 2(b)] was least-squares fitted with the model described in the previous section, using the experimentally determined T_{1e} values.

We note that the relaxation times measured with the VMT and VRT ENDOR experiments are not bulk relaxation times of H_α, but stem only from a subset of α-protons, namely, those that are in very close vicinity to a copper ion with an EPR resonance frequency matching the spectrometer frequency ω_{MW}.

IV. EXPERIMENTAL RESULTS

EPR spectrum. The echo-detected EPR spectrum of CuHis is shown in Fig. 3(a). It can be simulated assuming a single set of magnetic parameters $g_\parallel$=2.24, $g_\perp$=2.058, $A_\parallel$ =560 MHz, and $A_\perp \approx 50$ MHz, with a residual Gaussian broadening with 15 mT full width at half maximum.[7,19] At pH 7 and above, the major species is an octahedrally coordinated Cu(II) ion ligated by two histidines, with four N atoms in the equatorial plane,[7,20] as shown in Fig. 3(a), and possibly two O atoms from the carboxylate groups in the axial positions.[21]

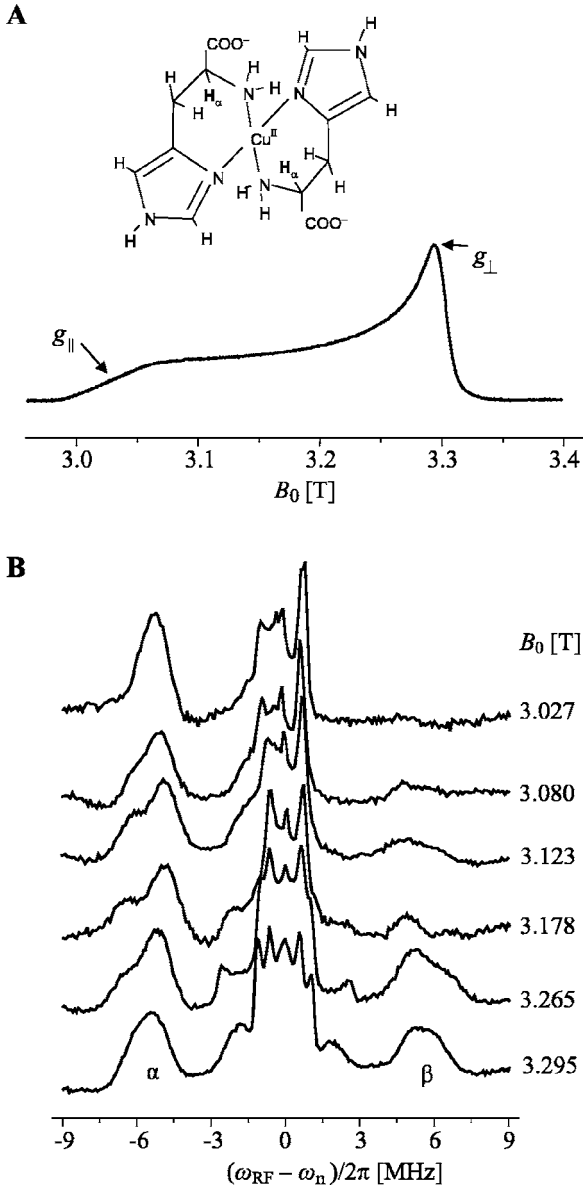

FIG. 3. 94.9 GHz EPR/ENDOR spectra of 2 mM CuHis at 5.5 K. (A) Structure of the complex and field swept echo-detected EPR spectrum, (B) field-dependent ^{1}H Davies ENDOR spectra recorded with t_R=15 ms and t_{mix}=1 μs.

ENDOR. The ^{1}H ENDOR spectrum of CuHis consists of two main signals, a well resolved doublet with a splitting of around 11 MHz assigned to the H_α proton and a powder pattern centered about the ^{1}H Larmor frequency, assigned to the H_ϵ proton.[7] The principal values of the hyperfine coupling tensor of H_α are $A_\parallel$=13.5 MHz and $A_\perp$=9.6 MHz, the angle between the $g_\parallel$ axis and the $A_\parallel$ axis is about 60°.[7]

Figure 2(a) shows the ENDOR spectrum of CuHis recorded at $g_\perp$ with short and long t_{mix} values. For t_{mix} =10 ms, the low-frequency H_α line has a negative amplitude ($F<0$), while its high-frequency counterpart amplitude is positive ($F>0$). This allows for the assignment of the low-frequency component to the α electron-spin manifold and therefore yields a positive hyperfine coupling for H_α. The spectrum recorded at short t_{mix}, 0.5 ms, exhibits some asymmetry with $F^\alpha > F^\beta$. This shows that the repetition time cho-

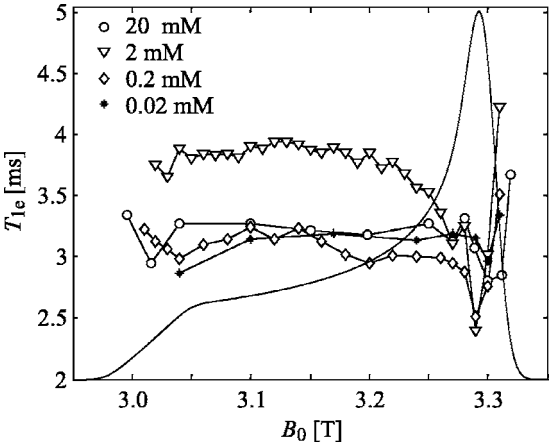

FIG. 4. The T_{1e} values of solutions of CuHis with different concentrations as a function of the magnetic field within the EPR powder pattern, measured at 94.9 GHz and 5.5 K.

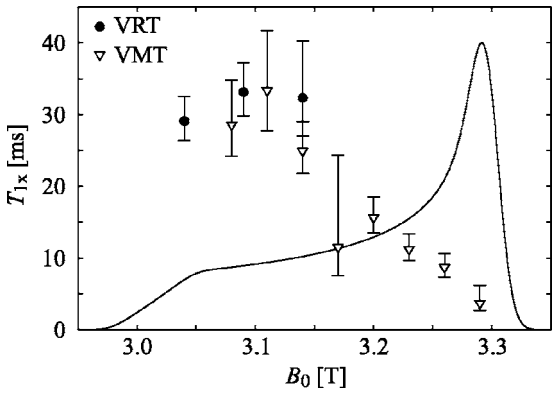

FIG. 5. The least-squares fitted T_{1x} values of H_α in 2 mM CuHis as a function of the magnetic field within the EPR powder pattern, measured at 94.9 GHz and 5.5 K. The error bars delimit the region where $\chi^2(T_{1x})$ is not more than 20% above the minimum value.

sen for these measurements, t_R=25 ms, is not sufficiently long to allow for full relaxation to thermal equilibrium. The full t_{mix} dependence of F^α and F^β is shown in Fig. 2(b).

^{1}H ENDOR spectra recorded at different magnetic field positions across the EPR powder pattern and with a short t_{mix} value ($t_{mix} \ll T_{1e}$) are presented in Fig. 3(b) and exhibit a highly field-dependent behavior. As the magnetic field increases from $g_\perp$ toward $g_\parallel$, the spectra become increasingly asymmetric. The spectrum recorded at $g_\parallel$ practically shows signals from only one electron-spin manifold. Here the asymmetry is a consequence of the saturation of the nuclear transitions and, as discussed above, the stronger signals are from the α manifold. These results show that ΔF is "anisotropic."

T_{1e} field dependence. Since ΔF depends on T_{1x}/T_{1e}, the field dependence of T_{1e} was measured. The T_{1e} values of CuHis, determined with the saturation recovery sequence, are depicted in Fig. 4 for concentrations in the range of 0.02–20 mM. The results show that the field dependence of T_{1e} is relatively small and evident only in the region of $g_\perp$, where a decrease is observed for all concentrations. The slightly higher T_{1e} values for the 2 mM sample are probably due to differences in the degassing procedure. The results show that, within the experimental accuracy, T_{1e} is practically concentration independent. Thus, the contribution of spectral diffusion, which is strongly concentration dependent, has been eliminated in the saturation recovery experiment.

T_{1x} field dependence. VMT and VRT ENDOR experiments were also carried out at different field positions within the EPR powder pattern and were analyzed by least-squares fitting the simple four-level model described above to the experimental data. In this analysis the T_{1e} values were taken from the saturation recovery experiments (Fig. 4) and $T_{1n}^{-1} \approx 0$ was assumed. The results obtained for the 2 mM solution for the H_α protons are shown in Fig. 5.

VMT experiments were performed over the entire spectral width except at the low-field edge, where the very low signal-to-noise ratio impeded the acquisition of analyzable data. In the VMT experiments, t_R was set to 25 ms in order to reduce acquisition time. With this t_R value, nuclear transitions in the $g_\parallel$ region are already partially saturated [see Fig. 3(b)]. This is taken into account in the analysis. VRT experiments were successful only at low fields, as no recovery curves could be obtained for the experimentally accessible range of t_R (10 ms and longer) in the $g_\perp$ region. For some field values both methods were used, yielding similar T_{1x} values.

The results show that T_{1x} is highly field dependent: while at $g_\parallel$ it is around 30 ms, it is ≈5 ms at $g_\perp$. Notably, the latter is on the same order of magnitude as T_{1e}. Unlike the field dependence of T_{1e}, which is rather small, that of T_{1x} is large, spanning almost an order of magnitude. The field dependence of T_{1x} is not unique to the H_α protons in the CuHis complex. Figure 3(b) shows that the asymmetry in the ENDOR signals of the H_ϵ protons increases significantly as the magnetic field at which the measurements are carried out approaches the value corresponding to $g_\parallel$. ^{1}H VMT and VRT ENDOR performed on other Cu(II) complexes, such as 2.0 mM $Cu(imidazole)_4^{2+}$ and $Cu(H_2O)_6^{2+}$, also show similar degrees of T_{1x} "anisotropy."

The concentration dependence of T_{1x} of H_α measured at field positions close to $g_\perp$ and $g_\parallel$ is shown in Fig. 6. At both

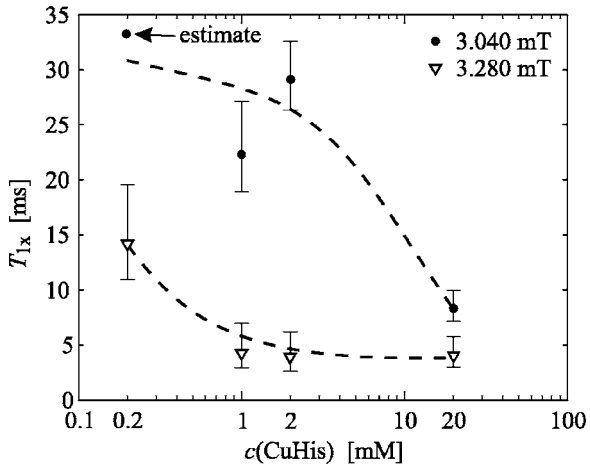

FIG. 6. The concentration dependence of T_{1x} of H_α in 2 mM CuHis, measured at $g_\parallel$ and $g_\perp$ and 5.5 K. The point labeled "estimate" is an estimated lower bound for T_{1x}. The error bars delimit the region where $\chi^2(T_{1x})$ is not more than 20% above the minimum value.

fields, T_{1x} approaches the value of T_{1e} as the concentration increases, but while for $g_\perp$ this occurs already at 1 mM, for $g_\parallel$ concentrations higher than 20 mM are required. The reported T_{1x} value at $g_\parallel$ for the 0.2 mM CuHis solution is an estimated lower bound as it was not possible to acquire ENDOR spectra with sufficiently high signal-to-noise ratio to permit a least-squares fit of the resulting data.

V. DISCUSSION

In the following we examine possible relaxation mechanisms that can bring the nuclear polarization back to thermal equilibrium and determine to what extent they contribute to the experimentally observed field and concentration dependence of T_{1x}.

The system at hand, an amorphous ensemble of dilute Cu(II) centers with an unpaired electron each in an environment of nuclear spins (ligand protons), can be described by the following spin Hamiltonian (in angular frequency units):

$$H = \mu_B \boldsymbol{B}_0 \boldsymbol{g}_i \boldsymbol{S}_i/\hbar - \gamma_n B_0 \boldsymbol{I}_{zk} + \boldsymbol{S}_i \boldsymbol{A}_{ij} \boldsymbol{S}_j + \boldsymbol{S}_i \boldsymbol{B}_{ik} \boldsymbol{I}_k + \boldsymbol{I}_k \boldsymbol{D}_{kl} \boldsymbol{I}_l, \tag{6}$$

where the sum over all electrons i,j and protons k,l is not explicitly shown. The first two terms represent the electron and nuclear Zeeman interactions, respectively, the third term the electron-electron dipolar interaction, the forth term represents the electron-nuclear hyperfine interaction, and the last term is the nuclear-nuclear dipole-dipole interaction responsible for the nuclear spin diffusion. At this stage we ignore the interaction between the electrons and their copper nuclei.

From the general spin Hamiltonian, we kept two electron spins, 1 and 2, and one nuclear spin 1 coupled to electron spin 1 and to all other nuclei k. At a high field, the nonsecular terms of the electron spins can be neglected, and we can write

$$\begin{aligned} H = {} & \omega_1(\Omega_1) S_{1z} + \omega_2(\Omega_2) S_{2z} + \omega_n I_{1z} + A_{zz} S_{1z} S_{2z} \\ & + A_\pm (S_{1+} S_{2-} + S_{1-} S_{2+}) + B_{zz} S_{1z} I_{1z} + B_{z+} S_{1z} I_{1+} \\ & + B^*_{z+} S_{1z} I_{1-} + \boldsymbol{I}_1 \boldsymbol{D}_{1k} \boldsymbol{I}_k, \end{aligned} \tag{7}$$

where $\omega_1(\Omega_1)$ and $\omega_2(\Omega_2)$ are the orientation-dependent resonance frequencies of the two electron spins, including the effects of their g tensor anisotropies and the Cu hyperfine interaction. ω_n is the nuclear Larmor frequency, $\omega_n = -\gamma_n B_0$. Note that in our case $|\omega_n| \gg |A|, |B|$. A_{zz}, $A_\pm$, B_{zz}, and B_{z+} are functions of the components of $\boldsymbol{A}$ and $\boldsymbol{B}$. In the ENDOR experiment, the spectrometer frequency ω_{MW} is set equal to ω_1. The terms neglected after the truncation are

$$\begin{aligned} & A_{z+}(S_{1z} S_{2+} + S_{1+} S_{2z}), \quad A^*_{z+}(S_{1z} S_{2-} + S_{1-} S_{2z}), \\ & B_{z+} S_{1+} I_{1z}, \quad B^*_{z+} S_{1-} I_{1z}, \quad B_\pm S_{1\pm} I_{1\mp}, \quad B_{2\pm} S_{1\pm} I_{1\pm}. \end{aligned} \tag{8}$$

All these terms connect energy levels separated by about ω_e, the electron Larmor frequency. Other neglected terms are $A_{2\pm} S_{1\pm} S_{2\pm}$, which connect energy levels separated by about $2\omega_e$.

While the terms retained in the high-field Hamiltonian determine the EPR and ENDOR spectra, those neglected can be a source of relaxation when their fluctuations induced by thermal motion or phonons have frequencies that are about equal to the transition frequencies ω_{nm} of this Hamiltonian. Relaxation mechanisms can, in general, be described by some fluctuating effective matrix elements $\langle n|X|m\rangle$, where $|n\rangle$ and $|m\rangle$ are nondegenerate eigenstates of the spin Hamiltonian describing the electron-nuclear spin system.[22] In this case the relaxation rates become proportional to the square of these effective matrix elements $|\langle n|X|m\rangle|^2$ and the value of the spectral density at the transition frequency ω_{nm}. The interactions generating these effective matrix elements are not necessarily represented by the terms in Eq. (8), but can originate, for example, from spin-phonon or spin-orbit interactions.[24]

A. Relaxation mechanisms involving up to two spins

T_{1e}-driven relaxation. A potentially significant relaxation mechanism is the so-called direct T_{1e} mechanism,[22,23] for which the relevant Hamiltonian terms are the pseudo- and nonsecular terms of the hyperfine coupling with spin operators shown in Eq. (8). As already mentioned, these terms, say, X, connect eigenstates of the secular Hamiltonian and can cause nuclear and cross relaxation when matrix elements of the type $\langle \alpha_1 \beta_n | X | \beta_1 \alpha_n \rangle$ or $\langle \alpha_1 \beta_n | X | \alpha_1 \alpha_n \rangle$ fluctuate at frequencies $\omega_1 \pm \omega_n$ or ω_n, respectively. Since the electron spin-lattice relaxation flips the electron spins at a rate of the order of T_{1e}^{-1}, which can be much larger than the actual thermal fluctuations, this T_{1e} replaces the correlation time of the actual thermal fluctuations of the nonsecular matrix elements. Thus an electron in the vicinity of the nucleus will accelerate the nuclear relaxation compared to nuclei in diamagnetic systems. This is often referred to as paramagnetic relaxation enhancement.[22,23] It is as well the basis for the solid effect in DNP.[22]

For a single electron-nuclear spin pair, this relaxation rate is[22,23]

$$T_{1x}^{-1} = \frac{1}{4} B_{z+}^2 \frac{1}{\omega_n^2 T_{1e}} (1 - P_0)^2, \tag{9}$$

where P_0 is the electron polarization $[P_0 = \tanh(\hbar \omega_{MW}/2\mu_B T)]$ and $\omega_n T_{1e} \gg 1$. The orientational dependence is given by $B_{z+} = (3/2)(\mu_0/4\pi)(\gamma_e \gamma_n / r_{en}^3) \sin 2\theta_n$, where θ_n is the angle between the external magnetic field and the electron-nucleus distance vector $\boldsymbol{r}_{en}$. A similar expression can be derived for the cross relaxation rate with the main difference that ω_n must be replaced by $\omega_e \pm \omega_n$.

The rate given by Eq. (9) is anisotropic due to the orientational dependence of T_{1e} and θ_n. Our experimental results show that the orientation dependence of T_{1e} is small and does not account for the observed field dependence of T_{1x} (see Fig. 4). In the CuHis complex, $\boldsymbol{r}$ forms an angle of about 60° with the $g_\parallel$ axis,[7] thus there will be a distribution of θ_n values for a given magnetic field (which selects spin systems mostly based on the angle θ_g between $\boldsymbol{B}_0$ and the $g_\parallel$ axis). Numerical computations yield distributions of θ_n as a function of θ_g or as a function of $\boldsymbol{B}_0$. The average of $\sin^2(2\theta_n)$ over these distributions shows a shallow minimum in the center of the spectrum, around $\theta_g \approx 50°$ or $B_0 \approx 3.15$ T. This

orientational dependence is thus different and less pronounced from the experimentally observed one.

In addition, evaluating Eq. (9) with the numbers relevant to our case, we obtain $T_{1x}^{-1}/T_{1e}^{-1} \leqslant 4\times 10^{-5}$. This ratio is much smaller than the experimentally found values of T_{1x}^{-1}/T_{1e}^{-1} between 0.1 and 1, so that this mechanism cannot make a significant contribution to the observed relaxation rate.

Nuclear spin diffusion. Another mechanism to be considered is the nuclear spin diffusion, which arises from the matrix elements of $\boldsymbol{D}_{1k}$ in Eq. (6). If energy-conserving flip flops of nuclear spins are possible, it can move polarization from the α histidine proton to protons farther away from the copper centers. This, however, requires the overlap of ^{1}H resonances. The ENDOR frequencies of H_α are isolated and lie within the nuclear diffusion barrier.[24] They do not overlap with ENDOR frequencies of any other proton. Protons from the amino group in the ligand could mediate the diffusion, but these have been exchanged for deuterium in our sample. Nonetheless, measurements carried out in a H_2O solution showed similar anisotropic behavior for the NH protons.[7] In this case there is a significant overlap between the ^{1}H resonances, hence we conclude that the nuclear spin diffusion does not dominate the relaxation process. On the other hand, this mechanism will certainly contribute to the spin-spin relaxations of the matrix protons[25] and of the histidine protons with small couplings.

B. Relaxation mechanisms involving two electron spins

So far, we have discussed relaxation mechanisms involving only a single paramagnetic center (unpaired electron and proton coupled to it). The observed concentration dependence suggests that there is a contribution from electron-electron interactions, and potential three-spin mechanisms have to be examined.[26,27] Thus we consider now a three-spin system consisting of the proton spin I, the excited electron spin S_1, and an additional distant electron spin S_2, described by the Hamiltonian given in Eq. (7). The diagonal elements of this Hamiltonian are determined by the Zeeman interactions and the electron-electron A_{zz} interaction term. The off-diagonal elements of the Hamiltonian, neglected in Eq. (7), are

$$\begin{aligned} |\langle\alpha_1\alpha_2\alpha_n|H|\alpha_1\beta_2\alpha_n\rangle| &= |\langle\beta_1\alpha_2\alpha_n|H|\beta_1\beta_2\alpha_n\rangle| = |A_{z\pm}/2|, \\ |\langle\alpha_1\alpha_1\alpha_n|H|\beta_1\alpha_2\alpha_n\rangle| &= |\langle\alpha_1\beta_2\alpha_n|H|\beta_1\beta_2\alpha_n\rangle| = |A_{\pm z}/2|. \end{aligned} \tag{10}$$

The magnitudes of these off-diagonal elements are much smaller than the difference between the corresponding diagonal elements, $|A_{z\pm}| \ll \omega_1, \omega_2$, justifying their removal. However, they could provide some proton relaxation mechanism, as we will discuss later. Additional off-diagonal elements, not neglected in Eq. (7), are

$$\begin{aligned} \langle\alpha_1\beta_2\alpha_n|H|\beta_1\alpha_2\alpha_n\rangle &= \langle\alpha_1\beta_2\beta_n|H|\beta_1 a_2\beta_n\rangle = A_\pm \\ |\langle\alpha_1\alpha_2\alpha_n|H|\alpha_1\alpha_2\beta_n\rangle| &= |\langle\alpha_1\beta_2\alpha_n|H|\alpha_1\beta_2\beta_n\rangle| = |B_{z\pm}/2|. \end{aligned} \tag{11}$$

The $A_\pm$ and $B_{z\pm}$ elements become significant when $A_\pm$ is on the order of $\Delta\omega = \omega_1 - \omega_2$ and $B_{z\pm}$ of the order of ω_n. In the first case the energies of the Hamiltonian are (neglecting $B_{zz} \ll \omega_n$)

$$\begin{aligned} E_{M=\pm1} &= +\tfrac{1}{4}A_{zz} \pm \tfrac{1}{2}\omega_n \pm \tfrac{1}{2}(\omega_1+\omega_2), \\ E_{M=0} &= -\tfrac{1}{4}A_{zz} \pm \tfrac{1}{2}\omega_n \pm \tfrac{1}{2}\sqrt{\Delta\omega^2 + 4A_\pm^2}. \end{aligned} \tag{12}$$

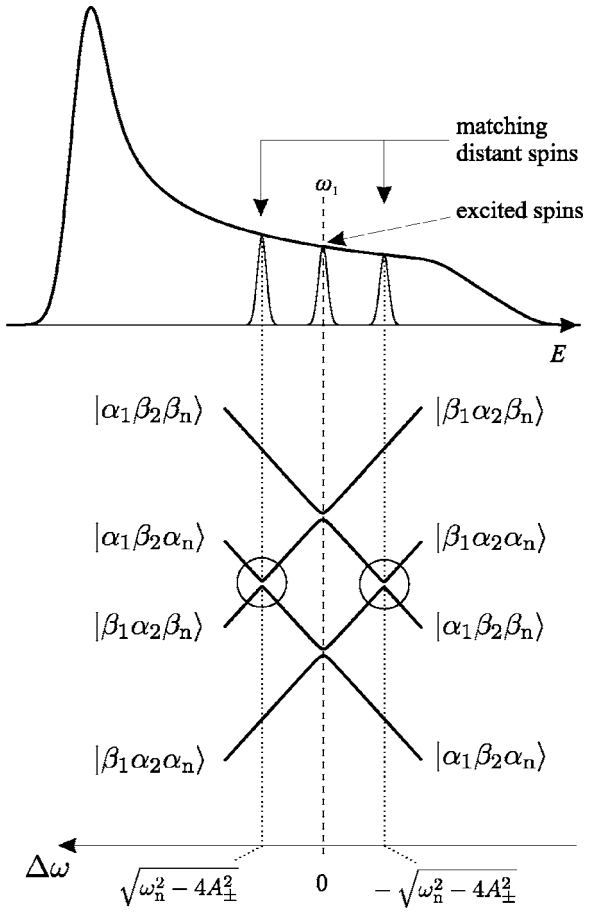

FIG. 7. Bottom: Energy level diagram as a function of $\Delta\omega = \omega_1 - \omega_2$ of an $S_1 = S_2 = I = 1/2$ spin system. Only states with antiparallel electron spins ($m_{S1} + m_{S2} = 0$) are shown; $\omega_n < 0$ and $|\omega_n| \gg |A_\pm|, |B_{z\pm}|, |B_{zz}|$ are assumed. Top: Calculated frequency-domain EPR spectrum of CuHis.

Figure 7 shows the energies $E_{M=0}$ of the four eigenstates with $M = m_{S1} + m_{S2} = 0$ as a function of the resonance frequency difference $\Delta\omega = \omega_1 - \omega_2$ of the electron spins. The eigenstates corresponding to these energies will show strong mixing when $\Delta\omega \approx 0$. Away from this condition the influence of $A_\pm$ on the eigenstates and their energies is minor. As long as $B_{z\pm} \ll \Delta\omega$, ω_n, its off-diagonal elements can be neglected as well. However, when degeneracies occur these elements can become significant. Such degeneracies occur when

$$\Delta\omega = \sqrt{\omega_n^2 - 4A_\pm^2}. \tag{13}$$

For $|\omega_n| \gg A_\pm$ (that is, at high fields and low concentrations), Eq. (13) reduces to $\Delta\omega \approx \pm\omega_n$. At $\Delta\omega = +\omega_n$, the corresponding energies become

$$E(|\alpha_1\beta_2\alpha_n\rangle; |\beta_1\alpha_2\beta_n\rangle) = -\tfrac{1}{4}A_{zz}, \tag{14}$$

$$E(|\alpha_1\beta_2\beta_n\rangle;|\beta_1\alpha_2\alpha_n\rangle) = -\tfrac{1}{4}A_{zz} \pm \omega_n,$$

and at $\Delta\omega = -\omega_n$ the energies are

$$E(|\alpha_1\beta_2\alpha_n\rangle;|\beta_1\alpha_2\beta_n\rangle) = -\tfrac{1}{4}A_{zz} \pm \omega_n,$$

$$E(|\alpha_1\beta_2\beta_n\rangle;|\beta_1\alpha_2\alpha_n\rangle) = -\tfrac{1}{4}A_{zz}. \tag{15}$$

In both cases the degeneracies can be lifted by the presence of off-diagonal elements from $B_{z\pm}$ and $A_\pm$. These elements can then be replaced, using degenerate perturbation theory, by

$$\langle\alpha_1\beta_2\alpha_n|H|\beta_1\alpha_2\beta_n\rangle = A_\pm B_{z+}/\omega_n,$$

$$\langle\alpha_1\beta_2\beta_n|H|\beta_1\alpha_2\alpha_n\rangle = A_\pm B_{z-}/\omega_n, \tag{16}$$

respectively. Relaxation in this spin system can originate from nonsecular off-diagonal terms $A_{z\pm}$, $A_{\pm z}$, and $A_\pm$ [Eqs. (10) and (11)], and $A_\pm B_{z\pm}/\omega_n$ [Eq. (16)]. Consequently, these matrix elements can provide a relaxation mechanism for the protons. In the case of the A coefficients their characteristic frequencies are at about ω_1, ω_2, and ω_n, respectively. The $A_{z\pm}$ coefficients can induce relaxation by fluctuations due to the electron spin-lattice relaxation rate, T_{1e}^{-1}, and the flip-flop terms $A_\pm$ by the electron-electron flip flops, T_{2e}^{-1}. If we assume that the spectral density is Lorentzian, we obtain an upper limit for these relaxation rates that is proportional to $(A_{z\pm}/\omega_1)^2 T_{1e}^{-1}$ and $(A_\pm/\omega_n)^2 T_{2e}^{-1}$ because $\omega_1^2 T_{1e}^2 \gg 1$ and $\omega_n^2 T_{2e}^2 \gg 1$. However, because $|A_{z+}|, |A_\pm| \ll |\omega_n| \ll \omega_1$ the resulting relaxation rate is much smaller than T_{1e}^{-1} and T_{2e}^{-1}. Therefore, this cannot account for the observed experimental $T_{1x}{}^{-1}$ relaxation rates.

The second three-spin relaxation mechanism, involving the effective matrix elements $A_\pm B_{z\pm}/\omega_n$, was previously used by van Houten *et al.*[26,27] to explain results from a saturation recovery NMR study (at fields between 0.3 and 1.5 T) on single crystals of a diluted copper tutton salt. There an orientation dependence of the ^{1}H nuclear relaxation rates similar to our experimental results was observed. They showed that at crystal orientations where the difference in frequency between the resonance lines from the two different Cu sites in the crystal is approximately equal to the nuclear Larmor frequency, there is an increase in the ^{1}H relaxation rate. The ^{1}H relaxation mechanism proposed in their work is based on the three-spin system described above, namely, a transition at the degeneracy condition Eq. (13) between the unmixed Zeeman states $|\alpha_1\beta_2\alpha_n\rangle$ and $|\beta_1\alpha_2\beta_n\rangle$ via the above mentioned off-diagonal matrix elements.

If such elements could cause relaxation, their contribution to the nuclear relaxation would have a magnitude on the order of $(A_\pm B_{z\pm}/\omega_n)^2$. For the experimental parameters used and the actual magnitudes of the hyperfine interactions, these effective matrix elements are very small and therefore we conclude that the transition probabilities evaluated by van Houten *et al.* are negligible in our case.

1. Direct T_{1e}-driven relaxation

Next we examine a third relaxation mechanism that is of different nature. The experimental fact that T_{1x}^{-1} can be of the order T_{1e}^{-1} suggests that T_{1x}^{-1} and T_{1e}^{-1} are driven by the same mechanism. As mentioned earlier, any mechanism of electron spin-lattice relaxation can be described by some effective dynamic coupling matrix element between the single electron states, $T_{1e}^{-1} \propto |\langle\alpha_{1,2}|X|\beta_{1,2}\rangle|^2$. In low-temperature EPR, $X(t)$ can originate from Raman, Orbach, and direct processes.[28]

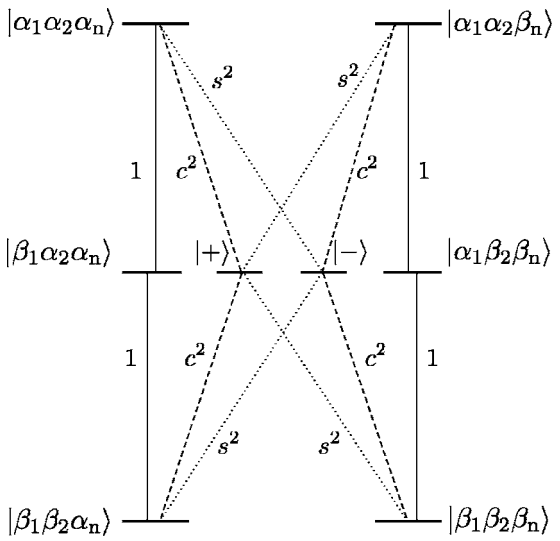

FIG. 8. Energy level diagram (assuming $|\omega_n| \ll \omega_{MW}$) for a three-spin system with matching electron spins ($\Delta\omega \approx \omega_n$). Lines connecting levels: transition rates for the relaxation matrix Γ_{een} in Eq. (20). The common prefactor Γ_e is omitted. c^2 and s^2 stand for $\cos^2\xi$ and $\sin^2\xi$, where ξ is given by Eq. (19). α_n (β_n) states are on the left (right), the mixed states $|+\rangle$ and $|-\rangle$ are in the center.

Under the conditions described by Eq. (13) an energy anticrossing can take place with a small energy splitting due to the matrix elements of Eq. (16), equal in first order to

$$\delta E \approx 2\left|\frac{A_\pm B_{z+}}{\omega_n}\right| \tag{17}$$

(see Fig. 7). The corresponding eigenstates, for $\Delta\omega \approx \omega_n$, are superpositions of pure Zeeman states,

$$|+\rangle = \cos\xi|\alpha_1\beta_2\alpha_n\rangle + \sin\xi|\beta_1 a_2\beta_n\rangle,$$

$$|-\rangle = \sin\xi|\alpha_1\beta_2\alpha_n\rangle - \cos\xi|\beta_1 a_2\beta_n\rangle, \tag{18}$$

with

$$\tan(2\xi) = (2A_\pm B_{z+}/\omega_n)/(\Delta\omega + \omega_n) \tag{19}$$

and similar expressions for $\Delta\omega \approx -\omega_n$. At the exact anticrossing, the coefficients become equal, $\cos\xi = \sin\xi = 2^{-1/2}$. Moving away from the anticrossing, the value of $\cos\xi$ approaches 1 and the states become pure product states.

As the states in Eq. (18) are linear combinations of Zeeman states, $X(t)$ connects them with pure Zeeman states, with matrix elements scaled down by $\cos\xi$ and $\sin\xi$. Accordingly, the relaxation rates for these transitions between Zeeman and mixed states are proportional to $T_{1e}^{-1}\cos^2\xi$ and $T_{1e}^{-1}\sin^2\xi$, as illustrated in Fig. 8, and involve frequencies of about ω_e or $\omega_e \pm \omega_n$.

All states in the system are now directly or indirectly connected by the electron spin-lattice relaxation mechanism,

allowing the nuclear polarization to relax when the levels are strongly mixed. This direct T_{1e}-driven mechanism can yield nuclear relaxation times which are of the same order of magnitude as the electron spin-lattice relaxation T_{1e}, as observed experimentally.

An analytical expression for the decay rate of the nuclear polarization, T_{een}^{-1}, for such a relaxation model can be derived. The relaxation matrix Γ_{een} for the three-spin system is

$$\Gamma_{een} = -\Gamma_e \begin{pmatrix} -2\epsilon & 0 & 1 & s^2 & c^2 & 0 & 0 & 0 \\ 0 & -2\epsilon & 0 & c^2 & s^2 & 1 & 0 & 0 \\ \epsilon & 0 & -1-\epsilon & 0 & 0 & 0 & 1 & 0 \\ \epsilon s^2 & \epsilon c^2 & 0 & -1-\epsilon & 0 & 0 & s^2 & c^2 \\ \epsilon c^2 & \epsilon s^2 & 0 & 0 & -1-\epsilon & 0 & c^2 & s^2 \\ 0 & \epsilon & 0 & 0 & 0 & -1-\epsilon & 0 & 1 \\ 0 & 0 & \epsilon & \epsilon s^2 & \epsilon c^2 & 0 & -2 & 0 \\ 0 & 0 & 0 & \epsilon c^2 & \epsilon s^2 & \epsilon & 0 & -2 \end{pmatrix}, \tag{20}$$

where the first row/column corresponds to the energy level lowest in energy and then in order of increasing energy (see Fig. 8). c^2 and s^2 stand for $\cos^2 \xi$ and $\sin^2 \xi$.

The eigenvalues κ_i of the relaxation matrix are the decay constants of the exponentials making up the multiexponential decay of an arbitrary population vector to equilibrium. The eigenvectors $\boldsymbol{V}_i$ represent the nature of the components of the population vector decaying with rates κ_i, so that the decay of a population vector can be written as

$$\boldsymbol{n}(t) = \sum_i c_i \exp(-\kappa_i t)\boldsymbol{V}_i, \tag{21}$$

where $c_i = \boldsymbol{n}(0)\cdot\boldsymbol{V}_i$. The eigenvalues of Γ_{een} are

$$\begin{aligned} \kappa_1 &= 0, \\ \kappa_2 &= \kappa_3 = \kappa_4 = \kappa_5 = (1+\epsilon)\Gamma_e, \\ \kappa_6 &= 2(1+\epsilon)\Gamma_e, \\ \kappa_7 &= [(1+\epsilon) - \sqrt{(1+\epsilon)^2 - 2\epsilon\sin^2(2\xi)}]\Gamma_e, \\ \kappa_8 &= [(1+\epsilon) + \sqrt{(1+\epsilon)^2 - 2\epsilon\sin^2(2\xi)}]\Gamma_e. \end{aligned} \tag{22}$$

Note that four of them are degenerate. The expressions for the associated eigenvectors are bulky. For the case $\epsilon=1$ (high-temperature limit) and $\epsilon=0$ (away from the anticrossings), they can be associated with the following population components: $\boldsymbol{V}_1$ is the part of the population that is at equilibrium, whereas $\boldsymbol{V}_2$ and $\boldsymbol{V}_3$ represent electron polarizations, S_{1z} and S_{2z}. $\boldsymbol{V}_4$ and $\boldsymbol{V}_5$ are the electron-nuclear two-spin orders $S_{1z}I_z$ and $S_{2z}I_z$. $\boldsymbol{V}_6$ describes the electron-electron two-spin order $S_{1z}S_{2z}$. $\boldsymbol{V}_7$ is the nuclear polarization I_z and $\boldsymbol{V}_8$ is the three-spin order $S_{1z}S_{2z}I_z$.

In the intermediate regime the simple population assignment is not possible and we are dealing with a complicated relaxation mechanism. However, it is clear that the slowest finite relaxation rate $T_{een}^{-1} = \kappa_7$ will form the cross relaxation bottleneck and must be compared with the electron spin-lattice relaxation rate $T_{1e}^{-1} = \kappa_2$. The ratio of these two constants is

$$\frac{T_{een}^{-1}}{T_{1e}^{-1}} \approx \left(1 - \frac{\sqrt{1+\epsilon^2}}{1+\epsilon}\right)\left[1 + \left(\frac{\Delta\omega \mp \omega_n}{2A_{\pm}B_{z+}/\omega_n}\right)^2\right]^{-1}, \tag{23}$$

where the trigonometric identity $\sin^2 x = (1+\tan^{-2} x)^{-1}$ and Eq. (19) were used.

This expression represents two Lorentzian functions of $\Delta\omega$, with centers at $\pm\omega_n$ and width of $(4/\sqrt{3})|A_{\pm}B_{z+}/\omega_n|$. They are zero far from the anticrossings, $|\Delta\omega \mp \omega_n| \gg 0$. At the anticrossings [see Eq. (13)], one of the two Lorentzians assumes its maximum value,

$$\left(\frac{T_{een}^{-1}}{T_{1e}^{-1}}\right)_{max} = 1 - \frac{\sqrt{1+\epsilon^2}}{1+\epsilon}. \tag{24}$$

This means that the relaxation mechanism is most effective when the two electron spins satisfy the matching condition in Eq. (13). As soon as there are electrons available which satisfy the matching condition, strong state mixing occurs and the electron spin-lattice relaxation enables the whole system, including the nucleus, to relax to thermal equilibrium. For decreasing temperature ($\epsilon \to 0$), the ratio in Eq. (24) decreases to zero, independent of ξ. For increasing temperature ($\epsilon \to 1$), it converges to $1-1/\sqrt{2} \approx 0.293$. For our experimental conditions, $\epsilon \approx 0.44$, so that

$$\left(\frac{T_{een}^{-1}}{T_{1e}^{-1}}\right)_{max} \approx 0.24. \tag{25}$$

Thus T_{een}^{-1} is of the same order as T_{1e}^{-1}, as we observed experimentally.

The overall relaxation rate due to this mechanism in a sample with many electron spins will of course depend on the concentration and on the availability of distant spins that

satisfy the matching condition in Eq. (13). For lower concentrations, less of such spins are available, and the relaxation of the nuclear polarization is expected to slow down, as was found in the experiment.

2. Monte Carlo simulations

In order to obtain a semiquantitative estimate of the overall nuclear relaxation rate due to the mechanism described above in our frozen solution of CuHis, we have to consider a disordered system consisting of many randomly oriented paramagnetic centers. For a sufficiently diluted system with a total of N electron spins, we assume that a particular nucleus coupled to an electron spin i with a resonance frequency ω_i will exhibit a relaxation rate T_{een}^{-1} determined effectively by only one electron spin j (with a resonance frequency ω_j) out of the remaining $(N-1)$ electrons, that best satisfies the matching condition in Eq. (13) and thus offers the largest ratio $\rho_{ij}=\rho_{\max,i}$, where $\rho_{ij}=(T_{\text{een}}^{-1}/T_{1\text{e}}^{-1})_{ij}$ as given by Eq. (23) and

$$A_{\pm,ij}(r_{ij},\theta_{ij})=\frac{\mu_0}{2\pi}\frac{(g_e\mu_B)^2}{\hbar}\frac{3\cos^2\theta_{ij}-1}{r_{ij}^3}, \tag{26}$$

where r_{ij} is the distance between spins i and j and θ_{ij} is the angle between the interspin vector and the z axis, and we neglect the g anisotropy. This gives $T_{\text{een},i}^{-1}=\rho_{\max,i}T_{1\text{e}}^{-1}$, where $T_{1\text{e}}^{-1}$ is the experimentally determined value. The nuclear polarization of this particular nucleus will relax according to $S_i(t)=\exp(-t/T_{\text{een},i})$.

To obtain the macroscopic relaxation rate, one then has to sum over all n possible configurations of the i electron-nucleus pairs, yielding the total normalized nuclear polarization decay,

$$S(t)=\frac{1}{n}\sum_i \exp(-t/T_{\text{een},i}). \tag{27}$$

In general, this overall relaxation function is not monoexponential. A stretched exponential $S_{\text{fit}}(t)=\exp[(-t/T_{\text{een}})^p]$ is fitted to it, with p and T_{een} as fitting parameters. The latter can then be compared to the experimentally determined $T_{1\text{x}}$.

The calculations were performed using a Monte Carlo approach as follows: $N-1$ electron spins j, corresponding to a concentration c, were placed in a cubic volume with edge length a using uniform random distributions in the x, y, and z coordinates. For a 2 mM solution, the average nearest-neighbor distance is about 10 nm. Each spin is assigned a random resonance frequency ω_i, using the nonuniform distribution obtained from the EPR spectral line shape for the given magnetic field B_0. At the center of the cube, an electron spin with resonance frequency $\omega_i=\omega_{\text{MW}}$ is placed. Spins that are closer than 1 nm to this central ENDOR spin are excluded since the Cu(II) ions of two CuHis complexes cannot approach much closer. For each spin j, the dipolar coupling $A_{\pm,ij}$ relative to the central spin i is computed. ρ_{ij} is then calculated using $B_{z+}=3$ MHz. A small broadening λ_0 is added to the Lorentzian width $\lambda_{\text{een},ij}=(4/\sqrt{3})A_{\pm,ij}B_{z+}/\omega_{\text{n}}$ in Eq. (23) in order to take into account the finite width of the ENDOR lines. This broadening, however, would allow very remote spins with $A_{\pm,ij}\approx 0$ but the right matching frequency to cause relaxation. This was circumvented by introducing a small threshold value $A_{\pm,\min}$, where spins with $|A_{\pm,ij}|$ below it are neglected. $A_{\pm,\min}$ was chosen so that the simulated low-field value of T_{een} was in the range of the the experimental value. The procedure was carried out several thousand times $(n=3000)$ for statistical averaging, and $S(t)$ was computed according to Eq. (27).

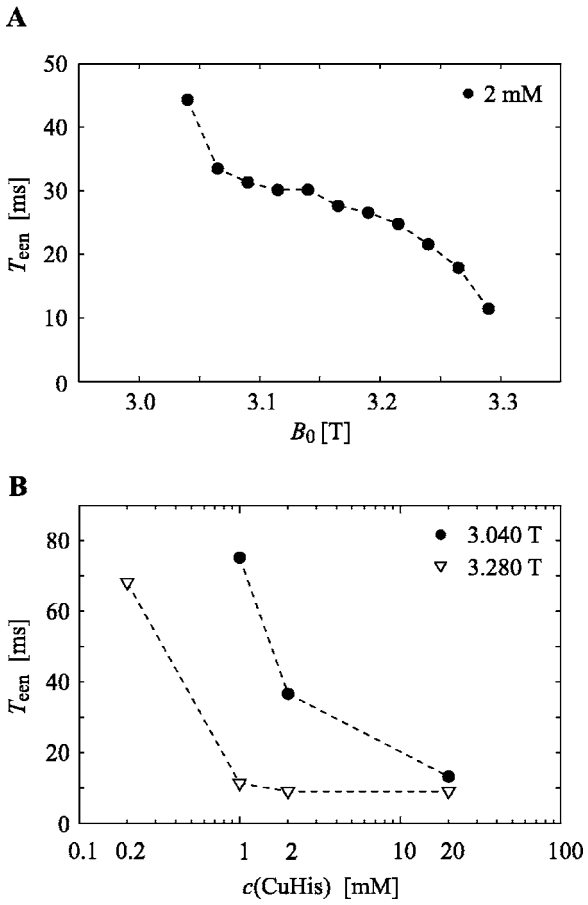

FIG. 9. (A) Simulated field dependence of the relaxation time T_{een} (experimental data in Fig. 5 (B) Simulated concentration dependence of T_{een} (experimental data in Fig. 6). Simulation parameters: concentration $c=2$ mM [for (A)], cube edge length $a=2$ μm, number of runs $n=3000$, dipolar threshold $A_{\pm,\min}=70$ kHz, and $\Delta\omega$ broadening $\lambda_0=1$ MHz.

The results of the Monte Carlo simulation of the field dependence of T_{een} are shown in Fig. 9(a). The decrease with increasing field is in good agreement with the experimental data from Fig. 5. The estimated values of T_{een} do not deviate by more than a factor of 4 from the experimentally determined $T_{1\text{x}}$ values, which can be considered reasonably accurate given the crudeness of both the models used for the data analysis and the simulation procedure. This indicates that the decay rate of the nuclear polarization is dominated by the direct $T_{1\text{e}}$-driven three-spin mechanism. However, less significant contributions due to other mechanisms cannot be ruled out.

Fitting the decay curves obtained from the Monte Carlo simulations with a stretched exponential yields p between 0.4 and 1, approaching the latter value as the concentration is increased. This exponent is a measure of the distribution of the mixing angles: the narrower the distribution, the closer to 1 is the exponent. The fact that stretched exponentials are

encountered here is not surprising, as they often appear in the form $\exp(-\sqrt{kt})$ in situations involving electron-electron cross relaxation.[29–31] Stretched exponentials are also known in resonance energy transfer.[32]

The agreement between the experimental and the simulated concentration dependence, shown in Fig. 9(b), supports the proposed mechanism as well. For low concentrations around 0.2 mM, the model predicts relaxation rates slower than those found experimentally, indicating that another relaxation mechanism might be contributing significantly in this regime. At high concentrations, the value of T_{1x} (T_{een}) at $g_{\|}$ approaches the one at $g_{\perp}$ both in the experimental and the simulated data.

These results can best be understood in terms of an effective concentration c_{eff} of the distant electron spins that satisfy the degeneracy condition [Eq. (13)]. The more such matching electron spins are available, the faster is the nuclear relaxation of the ENDOR spin. The decay rate increases with increasing c_{eff}. The effective concentration itself is proportional to the overall concentration and to the spectral densities at $\approx\omega_{MW}\pm\omega_n$, that is, to the amplitude of the EPR absorption spectrum. The higher these amplitudes, the higher the relaxation rates. There are more matching electrons in the $g_{\perp}$ spectral region than in the $g_{\|}$ region.

In our Monte Carlo simulation we took into account only three-spin systems. However, at higher concentrations it is expected that more than two electron spins can be involved, resulting in a speedup of the relaxation. We must therefore expect that at the high concentration side of our calculation the computed T_{een}^{-1} should be considered as a lower limit of the actual relaxation rate T_{1x}^{-1}. At the low concentration side, other relaxation mechanisms present in the system could contribute visibly to the overall relaxation rate, so that T_{een}^{-1} is again only a lower limit of T_{1x}^{-1}.

An electron-electron-nuclear three-spin mechanism has been used to account for dynamic nuclear polarization (DNP) at high field.[9] There it has been observed that the DNP strength increases with the electron-electron cross relaxation rate and thus with concentration.[10] In that work, electron-electron cross relaxation (and DNP) was observed for a 40 mM solution of 4-amino-2,2,6,6-tetramethylpiperidine-1-oxyl (4-amino-TEMPO), but not for a 1 mM solution. This has been recently further substantiated by showing that the DNP effect increases considerably when biradicals are used.[12] Another interesting manifestation of this mechanism has been observed for ^{15}N nuclear polarization buildup in optically detected EPR spectra of nitrogen vacancies next to nitrogen atoms in diamond.[33] This polarization was only found at magnetic fields where the matching condition described above in Eq. (13) is satisfied for the ^{15}N nucleus ($I=1/2$) and the two electron spins at the nitrogen atom ($S_1=1/2$) and the nitrogen vacancy ($S_2=1$), so that level anticrossings and strong state mixing result.

Interestingly, while the NH_2 protons of the CuHis complex exhibit strong asymmetry in the ^1H ENDOR spectrum similar to the α-protons, ^2H ENDOR of the ND_2 deuterons of the complex in a deuterated solvent, with the same concentration and recorded at the same temperature and the with the same repetition time, did not reveal any observable ENDOR asymmetry at any field position along the EPR powder pattern (data not shown).[7] Obviously the relaxation rate of the nuclear polarization is enhanced compared to the proton sample. However, Eq. (23) shows that the reduced gyromagnetic ratio should not affect T_{een}^{-1} because B_{z+}/ω_n remains constant. A different relaxation mechanism, probably due to the nonzero quadrupole interaction of deuterium, must therefore be responsible for the faster relaxation.

So far most studies of nuclear relaxation in paramagnetic systems were carried out by NMR spectroscopy, concentrating on remote protons, beyond the so-called diffusion barrier. The high-field VMT/VRT ENDOR experiments allow for exploration of the spin dynamics of nuclei within the diffusion barrier, namely, protons situated close to the unpaired electron having ENDOR frequencies that significantly deviate from the nuclear Larmor frequency. This can be further relevant to the understanding of electron-nuclear cross relaxation mechanisms at high fields and the optimization of the resulting DNP enhancement since the nuclei coupled to the electron spins are the first to be polarized, and then their polarization may spread via spin diffusion. Hence, their polarization decay rate may be an important factor.

VI. CONCLUSIONS

The overall relaxation rate of the histidine α-proton in a frozen solution of Cu(L-histidine)$_2$, measured at 94.9 GHz and at low temperature, has been shown to depend both on the magnetic field position within the EPR powder pattern and on the total spin concentration. This was accounted for by invoking a three-spin relaxation mechanism which is enabled by strong mixing of Zeeman states and driven by the same electron spin-lattice relaxation mechanism contributing to T_{1e}^{-1}. This causes relaxation of nuclear polarization that is on the order of T_{1e}^{-1}.

ACKNOWLEDGMENTS

This research has been supported by the Swiss National Science Foundation and by the Binational USA-Israel Science Foundation (BSF), Grant No. 2002175. D.G. holds the Erich Klieger Professorial Chair in Chemical Physics. S.V. holds the Joseph and Maria Robbins Professorial Chair. This work is made in part possible by the historic generosity of the Harold Perlman Family.

[1] D. Goldfarb and V. Krymov, in *Biological Magnetic Resonance*, edited by O. Grinberg and L. J. Berliner (Kluwer, New York, 2004), Vol. 22, p. 306.
[2] K. Möbius, A. Savitzky, M. Schnegg, M. Plato, and M. Fuchs, Phys. Chem. Chem. Phys. **7**, 19 (2005).
[3] M. Bennati and T. F. Prisner, Rep. Prog. Phys. **68**, 411 (2005).
[4] D. Goldfarb, Phys. Chem. Chem. Phys. **20**, 2325 (2006).
[5] M. T. Bennebroek and J. Schmidt, J. Magn. Reson. **128**, 199 (1997).
[6] B. Epel, A. Pöppl, P. Manikandan, S. Vega, and D. Goldfarb, J. Magn. Reson. **148**, 388 (2001).
[7] P. Manikandan, B. Epel, and D. Goldfarb, Inorg. Chem. **40**, 781 (2001).
[8] D. Goldfarb, B. Epel, H. Zimmermann, and G. Jeschke, J. Magn. Reson. **168**, 75 (2004).
[9] V. S. Bajaj, C. T. Farrar, I. Mastovsky, J. Vieregg, J. Byrant, B. Elena, K. E. Kreischer, R. J. Temkin, and R. G. Griffin, J. Magn. Reson. **160**, 85 (2003).
[10] C. T. Farrar, D. A. Hall, G. J. Gerfen, S. J. Inati, and R. G. Griffin, J. Chem. Phys. **114**, 4922 (2001).

[11] K.-N. Hu, V. S. Bajaj, M. Rosay, and R. G. Griffin, J. Chem. Phys. **126**, 044512 (2007).
[12] C. Song, K.-N. Hu, C.-G. Joo, T. M. Swager, and R. G. Griffin, J. Am. Chem. Soc. **128**, 11385 (2006).
[13] C. F. Hwang and D. A. Hill, Phys. Rev. Lett. **19**, 1011 (1967).
[14] A. Schweiger and G. Jeschke, *Principles of Pulse Electron Paramagnetic Resonance* (Oxford University Press, Oxford, 2001).
[15] A. M. Tyryshkin, J. J. L. Morton, A. Ardavan, and S. A. Loyd, J. Chem. Phys. **124**, 234508 (2006).
[16] W. Brüggemann and J. R. Niklas, J. Magn. Reson., Ser. A **108**, 25 (1994).
[17] B. Epel, D. Arieli, D. Baute, and D. Goldfarb, J. Magn. Reson. **164**, 78 (2003).
[18] I. Gromov, V. Krymov, P. Manikandan, D. Arieli, and D. Goldfarb, J. Magn. Reson. **139**, 8 (1999).
[19] S. Stoll and A. Schweiger, J. Magn. Reson. **178**, 42 (2006).
[20] D. Baute, D. Arieli, H. Zimmermann, F. Neese, B. M. Weckhuysen, and D. Goldfarb, J. Am. Chem. Soc. **126**, 11733 (2004).
[21] J. Gerbrand Mesu, T. Visser, F. Soulimani, E. E. van Faassen, P. de Peinder, A. M. Beale, and B. M. Weckhuysen, Inorg. Chem. **45**, 1960 (2006).
[22] A. Abragam and M. Goldman, Rep. Prog. Phys. **41**, 395 (1978).
[23] A. Abragam, *The Principles of Nuclear Magnetism* (Clarendon, Oxford, 1961).
[24] A. Abragam and M. Goldman, *Nuclear Magnetism: Order and Disorder* (Clarendon, Oxford, 1982), Chap. 6, p. 354.
[25] S. Schlick, L. Kevan, K. Toriyama, and M. Iwasaki, J. Chem. Phys. **74**, 282 (1981).
[26] J. van Houten, W. Th. Wenckebach, and N. J. Poulis, Physica B & C **92**, 201 (1977).
[27] J. van Houten, W. Th. Wenckebach, and N. J. Poulis, Physica B & C **92**, 210 (1977).
[28] A. Abragam and B. Bleaney, *Electron Paramagnetic Resonance of Transition Ions* (Dover, New York, 1970).
[29] T. Endo and T. Muramoto, Phys. Rev. B **29**, 6043 (1984).
[30] D. Tse and S. R. Hartmann, Phys. Rev. Lett. **21**, 511 (1968).
[31] P. M. Henrichs, M. L. Cofield, R. H. Young, and J. M. Hewitt, J. Magn. Reson. (1969-1992) **58**, 85 (1984).
[32] T. Förster, Z. Naturforsch. A **4A**, 321 (1949).
[33] T. Gaebel, M. Domhan, I. Popa, C. Wittmann, P. Neumann, F. Jelezko, J. R. Rabeau, N. Stavrias, A. D. Greentree, S. Prawer, J. Meijer, J. Twamley, P. R. Hemmer, and J. Wachtrup, Nat. Phys. **2**, 408 (2006).